remote sensing

MDPI

Article

LPI Sequences Optimization Method against Summation Detector Based on FFT Filter Bank

Qiang Liu, Fucheng Guo, Kunlai Xiong *, Zhangmeng Liu and Weidong Hu

The School of College of Electronic Science and Technology, National University of Defense Technology (NUDT), Changsha 410073, China; liuqiang17e@nudt.edu.cn (Q.L.); guofc@nudt.edu.cn (F.G.); liuzhangmeng@nudt.edu.cn (Z.L.); wdhu@nudt.edu.cn (W.H.)

* Correspondence: xiongkunlai@nudt.edu.cn

Abstract: Waveform design is a crucial factor in electronic surveillance (ES) systems. In this paper, we introduce an algorithm that designs a low probability of intercept (LPI) radar waveform. Our approach directly minimizes the detection probability of summation detectors based on FFT filter banks. The algorithm is derived from the general quadratic optimization framework, which inherits the monotonic properties of such methods. To expedite overall convergence, we have integrated acceleration schemes based on the squared iterative method (SQUAREM). Additionally, the proposed algorithm can be executed through fast Fourier transform (FFT) operations, enhancing computational efficiency. With some modifications, the algorithm can be adjusted to incorporate spectral constraints, increasing its flexibility. Numerical experiments indicate that our proposed algorithm outperforms existing ones in terms of both intercept properties and computational complexity.

Keywords: LPI; waveform design; unimodular sequences; propagation distance

Citation: Liu, Q.; Guo, F.; Xiong, K.; Liu, Z.; Hu, W. LPI Sequences Optimization Method against Summation Detector Based on FFT Filter Bank. *Remote Sens.* **2024**, *16*, 2021. https://doi.org/10.3390/rs16112021

Academic Editor: Andrzej Stateczny

Received: 17 April 2024
Revised: 27 May 2024
Accepted: 1 June 2024
Published: 4 June 2024

1. Introduction

During radar detection and tracking, the radar waveform is susceptible to detection, posing a significant threat to the radar's operation and survival [1,2]. As a result, radar systems continually demand advanced low-intercept technology. The objective is to develop a low probability of intercept (LPI) radar systems that can effectively detect targets while minimizing the likelihood of detection by ES systems [3]. This ensures enhanced security for both the radar system and its associated platforms.

Indeed, the concept of LPI radar was first developed in the 1980s [4]. Over the years, through iterative advancements, a plethora of low-interception technologies have progressively been implemented. Currently, the development of LPI radar primarily targets the two critical interception stages of the ES system: the power interception phase and the radar signature interception phase [5]. The power interception phase involves the ES's broad reception of all electromagnetic signals, detecting signals when their amplitude surpasses a certain threshold [6]. On the other hand, the radar signature interception phase refers to the process where the ES system extracts and identifies features from the detected signals [7].

The use of low-power continuous wave technology to diminish the chance of power interception is a superior low-interception method. It minimizes the peak of instantaneous power in the waveform by spreading the energy over an extended duration, thereby reducing the reconnaissance system's probability of interception [8,9]. Low-side-lobe antenna technology deliberately prevents the ES system from acquiring excess radiated energy, effectively preventing energy leakage and decreasing the interception likelihood [10]. Similarly, the dual/multi-station radar system reduces the interception probability by positioning the radar transmitter as far from the reconnaissance receiver as possible, thereby limiting the receiver's energy acquisition [11].

The frequency shortcut [12,13], pseudo-random [14], and complex waveform modulation techniques [15] are employed with the aim of reducing the interception probability of radar signatures. However, these techniques also inadvertently increase the processing complexity of the reconnaissance system. Furthermore, the issue of designing a low probability of identification (LPID) waveforms is being examined, with a specific focus on the aspect of time complexity [16,17].

The aforementioned tools for low-interception do not delve into the potential influence that waveform design could have on low-interception performance. In reality, waveform design is a crucial method for impacting ES systems [18]. The design of LPI radar waveforms has been employed as a countermeasure against ES systems as far back as the 1990s [19,20]. Among the various techniques, shortening the parameters of the waveform is an effective low-intercept method that targets the reduction in feature interception probability [21,22].

The swift fluctuation in radar waveform parameters makes it difficult for the receiver to accurately identify the relevant parameters of the waveform, which in turn obstructs effective classification and identification [23]. Furthermore, the advent of innovative radar systems has led to a heightened degree of versatility in waveform design [24]. The development of these cutting-edge radar systems primarily focuses on MIMO radar waveform design, utilizing waveform diversity to boost the adaptability of LPI radar waveform design. The incorporation of transmit beamforming further enhances the radar's stealth detection capabilities [25].

Nonetheless, as processing power improves, an increasing number of reconnaissance systems can intercept complex waveforms. They achieve this by analyzing and extracting suspicious features from the received signals [26,27]. Even under low signal-to-noise ratio conditions, contemporary low-interception systems are capable of identifying the potential characteristics of radar waveforms [28].

In recent years, a number of scholars have utilized Kullback–Leibler (KL) divergence for the measurement to represent the feature interception and identification process of radar missions and ES systems, which takes into account the detection characteristics under the joint entropy constraint for LPI waveform design, aiming to make the reconnaissance system lose more information [29,30]. However, simply utilizing the clustering and dispersion characteristics of the frequency domain distribution is not well adapted to the characteristics of modern wide-band ES systems [31,32].

To better obscure waveform features and enhance detection capabilities, a waveform design method was developed. This method conceals the spectral features of the waveform within the spectral features of the background noise. Under a specific received signal-to-noise ratio, the discrepancy between the periodic spectrum of the designed waveform and that of the Gaussian white noise is minimized. This minimization increases the complexity of feature extraction for reconnaissance receivers, thereby boosting the waveform's low-interception performance.

Waveform design methods aimed at reducing the probability of power interception in LPI radar initially distribute signal power over a wider frequency band using pulse compression theory [33,34]. The advent of new regime radars then amplified the signal's bandwidth, resulting in a wider signal bandwidth and a larger frequency range for energy distribution. Furthermore, MIMO radar waveform design minimizes the peak power captured by the interception system through the transmission beamforming technique [35,36]. The emergence of advanced frequency diversity array (FDA) radars [37], which utilize electronically scanned methods, further broadened the technical scope of LPI radar waveform design research.

Undeniably, diminishing the peak radiated power of passive reconnaissance systems is an efficacious method for low interception. However, this leads to a decline in detection performance as the energy radiated at the target diminishes. Therefore, target detection with low radiated power is typically accomplished through energy accumulation over the duration of the pulse train, which unfortunately compromises radar sensitivity.

Detecting signals that are embedded in the radio spectrum is a common challenge in various applications, including spectrum detectors in cognitive radio systems [38], cognitive radar systems [39], and ES systems [40]. More specifically, the challenge involves detecting signals within a spectrum using a receiver that has an instantaneous bandwidth (IBW).

One possible solution for this challenge is to use the total power radiometer [41], also known as the energy detector. This detector does not require a calculated frequency spectrum and compresses the entire band (i.e., the samples) into a single detection variable. This variable is then compared to a detection threshold. However, the frequency resolution of these detectors is limited to the entire IBW.

Another type of detector involves calculating the detection variable for each band in the digital spectrum, which is then compared to a threshold [42]. The frequency resolution of these detectors is limited to the bandwidth of the band.

We chose to use the FFT filter bank-based summation detector, which is a modified version of the basic FFT filter bank detector [43]. The FFT summation detector groups FFT bins to correspond with the desired channelization and estimates the power contained in each channel by summing the power computed for the individual bins.

In this paper, we present the MPI (monotonic minimizer for the probability of intercept) algorithm, which is designed to efficiently reduce the detection probability of summation detectors based on FFT filter banks in a monotonic manner. The MPI algorithm is derived by applying a general quadratic optimization framework method to the probability of intercept minimization problem, resulting in a simple closed-form solution at each iteration. The power method-like iteration (PMLI) formulation, as mentioned in [44], provides valuable guarantees regarding the convergence of the waveform itself. Furthermore, the algorithm's implementation is computationally efficient due to the utilization of fast Fourier transform (FFT). However, the nature of the unimodular constraint may lead to the slow convergence of the MPI algorithm, particularly for large lengths. To address this issue, we propose the application of acceleration schemes based on the squared iterative method (SQUAREM). Additionally, for scenarios involving spectral and similarity constraints, we developed a modified algorithm of a similar form.

2. Problem Formulation

Figure 1 shows the LPI radar and ES system framework. Conventional LPI radars employ a generalized low-intercept design scheme, including power control, complex modulation, and ultra-low sidelobe, to make it more difficult to process the radar signal at the ES side. This achieves LPI potency to some extent.

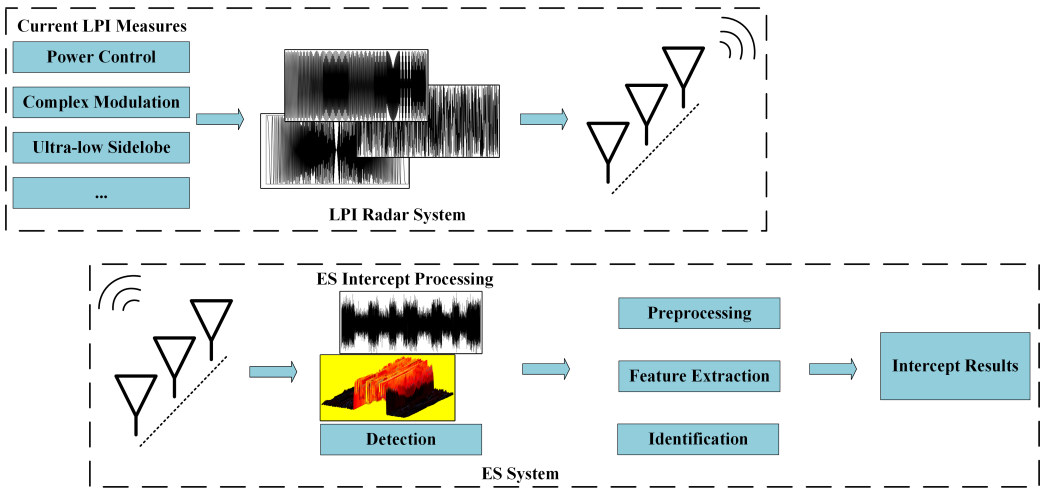

Figure 1. The sketch of the LPI radar and ES system framework.

The problem of interest is to design a complex unimodular sequence $\{s_n\}_{n=1}^{N}$, where N is the length of the sequence, minimizing the probability of detection P_d, i.e.,

$$\begin{cases} \min\limits_{\boldsymbol{s}} P_d \\ s.t.\ \ |s_n| = 1, n = 0, ..., N-1 \end{cases} \tag{1}$$

Next, we will restate Equation (1) from the perspective of a summation detector based on an FFT filter bank detection algorithm.

2.1. Receiver Signal Detection

Assuming that there are M channels in the sampled bandwidth, which are uniformly distributed in frequency, an integer number of K FFT bins are assigned per channel for power estimation. Therefore, an FFT of length $M \times K$ is required to compute the power for the M channels. Let $\mathbf{W}$ be the diagonal matrix consisting of a linear-phase FIR filter of length MK, which can be expressed as $\mathbf{W} = \text{Diag}[w_1, ..., w_{MK}]^{\text{T}}$.

Under the assumption of a complex Gaussian white noise background and a distribution where $\boldsymbol{n}$ follows a mean of 0 and a variance of σ_n^2, the received signal consists of a combination of $\boldsymbol{n}$ and $\boldsymbol{s}$. After down-conversion, the received vector $\boldsymbol{r} = [r_1, r_2, ..., r_{(P-1)(1-\gamma)\text{MK}+\text{MK}}]$ is divided into P overlapping sample vectors $\boldsymbol{r}_1, ..., \boldsymbol{r}_P$ as follows:

$$\boldsymbol{r}_m = \left[r_{m(1-\gamma)MK+1}, r_{m(1-\gamma)MK+2}, ..., r_{m(1-\gamma)MK+MK} \right]^{\text{T}} \tag{2}$$

where each vector $\boldsymbol{r}_m$ has γMK samples in common with the preceding vector $\boldsymbol{r}_{m-1}$ and $0 \leq \gamma < 1$ is overlapping ratio. The step length can be expressed as $L = (1-\gamma)MK$. The vector $\boldsymbol{r}_m$ is windowed by the FIR filter matrix $\mathbf{W}$, resulting in the windowed sample vector $\boldsymbol{x}_m$:

$$\boldsymbol{x}_m = [w_1 r_{mL+1}, w_2 r_{mL+2}, ..., w_{MK} r_{mL+MK}]^{\text{T}} \tag{3}$$

For the simplicity of expression, define the selection matrix $\mathbf{J}_p$, which can be expressed as:

$$\mathbf{J}_p = \left[\mathbf{0}^{MK \times (p-1)L} \quad | \quad \mathbf{I}_{MK} \quad | \quad \mathbf{0}^{MK \times (P-p)L} \right] \tag{4}$$

where $\mathbf{I}_{MK}$ is a unit diagonal matrix of dimension MK. The detection variable κ_m for the mth channel of the FFT filter bank-based summation detector is expressed as [45]:

$$\begin{aligned} \kappa_m =& \frac{1}{P} \sum_{p=1}^{P} (\mathbf{C}_m^{\text{H}} \mathbf{W} \mathbf{J}_p \boldsymbol{r})^{\text{H}} (\mathbf{C}_m^{\text{H}} \mathbf{W} \mathbf{J}_p \boldsymbol{r}) \\ =& \frac{p_s}{P} \sum_{p=1}^{P} (\mathbf{C}_m^{\text{H}} \mathbf{W} \mathbf{J}_p \boldsymbol{s})^{\text{H}} (\mathbf{C}_m^{\text{H}} \mathbf{W} \mathbf{J}_p \boldsymbol{s}) + c_m \end{aligned} \tag{5}$$

where $\mathbf{C}_m = [\boldsymbol{\alpha}_{(m-1)K}, ..., \boldsymbol{\alpha}_{mK-1}]^{\text{T}}$ and $\boldsymbol{\alpha}_k = 1/(MK) \cdot [1, e^{j\frac{2\pi k}{MK}}, ..., e^{j\frac{2\pi k(MK-1)}{MK}}]^{\text{T}}$. In addition, p_s is the received power of $\boldsymbol{s}$ and the scalar c_m represents the detection scalar associated with noise. When the influence of filters is disregarded, $\mathbb{E}\{c_m\} = \frac{1}{M}\sigma_n^2$, where $\mathbb{E}\{\cdot\}$ is the operator for mean. A signal is declared to exist in the mth channel only if $\kappa_m \geq \mu_{th}$, where μ_{th} is the detection threshold. It should be noted that adjusting the value of μ_{th} can achieve the desired false alarm probability P_{fa}.

In the case where the detection threshold μ_{th} and σ_n^2 is fixed, the waveform design problem for LPI in the mth channel can be expressed as $\min\limits_{\boldsymbol{s}} \kappa_m$. The detection vector $\boldsymbol{\kappa}$ is defined as a column vector comprising the elements $\kappa_1, \kappa_2, ..., \kappa_M$. Therefore, the output signal-to-noise ratio (SNR) of the mth channel can be expressed as:

$$SNR_m = \frac{p_s \sum_{p=1}^{P} (\mathbf{C}_m^{\text{H}} \mathbf{W} \mathbf{J}_p \boldsymbol{s})^{\text{H}} (\mathbf{C}_m^{\text{H}} \mathbf{W} \mathbf{J}_p \boldsymbol{s})}{P c_m} \tag{6}$$

The maximum output SNR of all channels is equal to the total output SNR of the FFT filter bank-based summation detector. Assuming uniform noise levels across all channels, the waveform design problem for LPI scenarios can be succinctly formulated as $\min_{\boldsymbol{s}} \max_{m} \kappa_m, m = 1, ..., M$. Consequently, the LPI problem (1) becomes

$$\begin{cases} \min\limits_{\boldsymbol{s}} & \|\boldsymbol{\kappa}\|_\infty \\ s.t. & |s_n| = 1, n = 0, ..., N-1 \end{cases} \tag{7}$$

where $\|\cdot\|_\infty$ is the infinity norm operator.

2.2. LPI Radar Waveform Design

Assuming that the optimization variable $\boldsymbol{s}$ is an N-dimensional vector, where N equals $MK + (P-1)L$, without loss of generality. In this case, we can disregard the energy distortion caused by FIR filters and noise, and set $\mathbf{W}$ equal to the identity matrix $\mathbf{I}$. Then, the sufficiency problem of Equation (7) can be formulated as follows (as proven in Appendix A):

$$\begin{cases} \min\limits_{\boldsymbol{s}} \max\limits_{m,p} & (\mathbf{C}_m^{\mathrm{H}} \mathbf{J}_p \boldsymbol{s})^{\mathrm{H}} (\mathbf{C}_m^{\mathrm{H}} \mathbf{J}_p \boldsymbol{s}) \\ s.t. & |s_n| = 1, n = 0, ..., N-1 \end{cases} \tag{8}$$

According to Parseval's theorem, $\sum_{m=1}^{M} (\mathbf{C}_m^{\mathrm{H}} \mathbf{J}_p \boldsymbol{s})^{\mathrm{H}} (\mathbf{C}_m^{\mathrm{H}} \mathbf{J}_p \boldsymbol{s}) = MK$ and it can be further obtained that $0 \leq \max\limits_{m,p} (\mathbf{C}_m^{\mathrm{H}} \mathbf{J}_p \boldsymbol{s})^{\mathrm{H}} (\mathbf{C}_m^{\mathrm{H}} \mathbf{J}_p \boldsymbol{s}) \leq MK$. The optimal value of Equation (8) must be greater than K; hence, the equivalence problem for Equation (8) can be formulated as follows:

$$\begin{cases} \min\limits_{\boldsymbol{s}} & \sum_{m=1}^{M} \sum_{p=1}^{P} \|(\mathbf{C}_m^{\mathrm{H}} \mathbf{J}_p \boldsymbol{s})^{\mathrm{H}} (\mathbf{C}_m^{\mathrm{H}} \mathbf{J}_p \boldsymbol{s}) - K\|^2 \\ s.t. & |s_n| = 1, n = 0, ..., N-1 \end{cases} \tag{9}$$

It is important to note that the number of channels is not a priori information, and therefore, Equation (9) can be formulated more appropriately as follows:

$$\begin{cases} \min\limits_{\boldsymbol{s}} & \sum_{m=1}^{MK} \sum_{p=1}^{P} \|(\boldsymbol{\alpha}_m^{\mathrm{H}} \mathbf{J}_p \boldsymbol{s})^{\mathrm{H}} (\boldsymbol{\alpha}_m^{\mathrm{H}} \mathbf{J}_p \boldsymbol{s}) - 1\|^2 \\ s.t. & |s_n| = 1, n = 0, ..., N-1 \end{cases} \tag{10}$$

Expanding the square in the objective function yields:

$$\begin{cases} \min\limits_{\boldsymbol{s}} & \sum_{m=1}^{MK} \sum_{p=1}^{P} (((\boldsymbol{\alpha}_m^{\mathrm{H}} \mathbf{J}_p \boldsymbol{s})^{\mathrm{H}} (\boldsymbol{\alpha}_m^{\mathrm{H}} \mathbf{J}_p \boldsymbol{s}))^2 \\ & \qquad -2(\boldsymbol{\alpha}_m^{\mathrm{H}} \mathbf{J}_p \boldsymbol{s})^{\mathrm{H}} (\boldsymbol{\alpha}_m^{\mathrm{H}} \mathbf{J}_p \boldsymbol{s}) + 1) \\ s.t. & |s_n| = 1, n = 0, ..., N-1 \end{cases} \tag{11}$$

Using Parseval's theorem, it can be shown that the second term in the objective function is a constant, i.e., $\sum_{m=1}^{MK} \sum_{p=1}^{P} (\boldsymbol{\alpha}_m^{\mathrm{H}} \mathbf{J}_p \boldsymbol{s})^{\mathrm{H}} (\boldsymbol{\alpha}_m^{\mathrm{H}} \mathbf{J}_p \boldsymbol{s}) \equiv PMK$. Therefore, by ignoring the constant terms, the problem can be simplified as follows:

$$\begin{cases} \min\limits_{\boldsymbol{s}} & \sum_{m=1}^{MK} \sum_{p=1}^{P} ((\boldsymbol{\alpha}_m^{\mathrm{H}} \mathbf{J}_p \boldsymbol{s})^{\mathrm{H}} (\boldsymbol{\alpha}_m^{\mathrm{H}} \mathbf{J}_p \boldsymbol{s}))^2 \\ s.t. & |s_n| = 1, n = 0, ..., N-1 \end{cases} \tag{12}$$

Let us denote the sliding window matrix as $\mathbf{S}$.

$$\mathbf{S} = \begin{bmatrix} \mathbf{J}_1 \boldsymbol{s} & | & \cdots & | & \mathbf{J}_P \boldsymbol{s} \end{bmatrix} \tag{13}$$

Equation (12) can be rewritten as

$$\begin{cases} \min\limits_{s} & \sum_{m=1}^{MK}((\boldsymbol{\alpha}_m^{\mathrm{H}}\mathbf{S})^{\mathrm{H}}(\boldsymbol{\alpha}_m^{\mathrm{H}}\mathbf{S}))^2 \\ s.t. & |s_n| = 1, n = 0, ..., N-1 \end{cases} \tag{14}$$

For the sake of better expression, let us define $\mathbf{X} = \mathbf{S}\mathbf{S}^{\mathrm{H}}$ and $\mathbf{A}_m = \boldsymbol{\alpha}_m\boldsymbol{\alpha}_m^{\mathrm{H}}$. With these definitions, Equation (12) can be rewritten as:

$$\begin{cases} \min\limits_{s} & \sum_{m=1}^{MK}\mathrm{Tr}(\mathbf{X}\mathbf{A}_m)^2 \\ s.t. & |s_n| = 1, n = 0, ..., N-1 \end{cases} \tag{15}$$

It is worth noting that Equation (15) changes the quartic function on $\mathbf{S}$ into a quadratic function on $\mathbf{X}$.

2.3. Optimization Problem

The optimization problem for LPI radar waveform design against a summation detector based on FFT filter bank, as denoted by (15), lacks the capability to construct a fuzzy function for the waveform. This limitation prevents the guarantee of certain desirable properties, such as a lower integrated sidelobe level (ISL).

Similarity constraints refer to the requirement that the designed waveform has a certain degree of similarity or correlation among its different components. Several studies have shown that enforcing a similarity constraint on a waveform can control the shape of its ambiguity function [46,47], partially circumventing issues such as significant modulus variation, poor range resolution, and/or high peak sidelobe levels. In Equation (15), we consider the following similarity constraint:

$$\|\hat{\mathbf{s}} - \boldsymbol{s}_0\|_\infty \leq \xi \tag{16}$$

where $\boldsymbol{s}_0$ denotes the reference waveforms, ξ is a use-specific parameter which rules the size of similarity region. For a given $\xi > 0$, (16) can be transformed into the following optimization problem:

$$\begin{cases} \min\limits_{s} & \sum_{m=1}^{MK}\mathrm{Tr}(\mathbf{X}\mathbf{A}_m)^2 \\ s.t. & |s_n| = 1, n = 0, ..., N-1 \\ & \|\hat{\mathbf{s}} - \boldsymbol{s}_0\|_\infty \leq \xi \end{cases} \tag{17}$$

Furthermore, in practical applications, radar systems must satisfy spectral constraints in addition to having good autocorrelation properties. For example, certain spectral powers must be below specified levels.

Spectral constraints, such as limiting the power in a certain frequency band, denoted by the set of indices $\Omega \subset [1, MK]$, can be expressed as follows: the power in Ω should be lower than a certain threshold ϵ.

$$\sum_{k\in\Omega}\|\boldsymbol{\alpha}_k^{\mathrm{H}}\mathbf{S}\|_2^2 \leq \epsilon \tag{18}$$

From (16) and (18), the optimization problem (15) can be rewritten as:

$$\begin{cases} \min\limits_{s} & \sum_{m=1}^{MK}\mathrm{Tr}(\mathbf{X}\mathbf{A}_m)^2 \\ s.t. & |s_n| = 1, n = 0, ..., N-1 \\ & \|\hat{\mathbf{s}} - \boldsymbol{s}_0\|_\infty \leq \xi \\ & \sum_{k\in\Omega}\|\boldsymbol{\alpha}_k^{\mathrm{H}}\mathbf{S}\|_2^2 \leq \epsilon \end{cases} \tag{19}$$

3. Optimization Development

In this section, we develop an algorithm for LPI waveform design based on the general quadratic optimization framework.

3.1. Monotonic Minimizer for Probability of Intercept

As $\mathrm{Tr}(\mathbf{X}\mathbf{A}_m) = \mathrm{vec}(\mathbf{X})^{\mathrm{H}} \cdot \mathrm{vec}(\mathbf{A}_m)$, Equation (15) can be considered as a quadratic optimization problem of generic form as follows:

$$\begin{cases} \min\limits_{\boldsymbol{s}} & \mathrm{vec}(\mathbf{X})^{\mathrm{H}} \boldsymbol{\Phi} \mathrm{vec}(\mathbf{X}) \\ s.t. & |s_n| = 1, n = 0, ..., N-1 \end{cases} \tag{20}$$

where $\boldsymbol{\Phi}$ is a positive definite and $\boldsymbol{\Phi} = \sum_{m=1}^{MK} \mathrm{vec}(\mathbf{A}_m) \cdot \mathrm{vec}(\mathbf{A}_m)^{\mathrm{H}}$. Because of $\boldsymbol{\Phi} \preceq \mathbf{I}$, Equation (20) is NP-hard for the constraint set [48,49]. A monotonically decreasing objective of (20) can be achieved by iteratively updating $\mathrm{vec}(\mathbf{X})$ by solving the following nearest problem at each iteration, where $\mathbf{G} = \boldsymbol{\Phi} - \mathbf{I}$:

$$\begin{cases} \max\limits_{\boldsymbol{s}} & \|\mathrm{vec}(\mathbf{X}) - \mathbf{G}\mathrm{vec}(\mathbf{X})^{(i)}\|_2 \\ s.t. & |s_n| = 1, n = 0, ..., N-1 \end{cases} \tag{21}$$

where $\mathbf{X}^{(i)} = \mathbf{S}^{(i)}(\mathbf{S}^{(i)})^{\mathrm{H}}$ at iteration k. However, according to (21), $\mathrm{vec}(\mathbf{X})$ is a quadratic form of $\mathrm{vec}(\mathbf{S})$, unimodular constraints are equivalent to making the $(p-1)MK + p$th element of $\mathrm{vec}(\mathbf{X})$ equal to MK. To solve the problem given in Equation (21), an efficient way is to expand it as follows:

$$\begin{cases} \max\limits_{\boldsymbol{s}} & \mathrm{vec}(\mathbf{X})^{\mathrm{H}}\mathrm{vec}(\mathbf{X}) - 2\mathrm{Re}(\mathrm{vec}(\mathbf{X})^{\mathrm{H}}\mathbf{G}\mathrm{vec}(\mathbf{X}^{(i)})) \\ & + \mathrm{vec}(\mathbf{X}^{(i)})^{\mathrm{H}}(\mathbf{G}^{\mathrm{H}}\mathbf{G})\mathrm{vec}(\mathbf{X}^{(i)}) \\ s.t. & |s_n| = 1, n = 0, ..., N-1 \end{cases} \tag{22}$$

Additionally, we have $MKP^2 \leq \mathrm{vec}(\mathbf{X})^{\mathrm{H}} \cdot \mathrm{vec}(\mathbf{X}) \leq (MKP)^2$ (proof in Appendix B), which is just a constant. After ignoring the constant term in Equation (23), the majorized problem of Equation (22) is given by:

$$\begin{cases} \min\limits_{\boldsymbol{s}} & \mathrm{Re}(\mathrm{vec}(\mathbf{X})^{\mathrm{H}}\mathbf{G}\mathrm{vec}(\mathbf{X}^{(i)})) \\ s.t. & |s_n| = 1, n = 0, ..., N-1 \end{cases} \tag{23}$$

which can be rewritten as

$$\begin{cases} \min\limits_{\boldsymbol{s}} & \sum_{m=1}^{MK} \mathrm{Re}(\mathrm{Tr}(\mathbf{X}^{(i)}\mathbf{A}_m) \cdot \mathrm{Tr}(\mathbf{X}\mathbf{A}_m)) - \mathrm{Tr}(\mathbf{X}^{(i)}\mathbf{X}) \\ s.t. & |s_n| = 1, n = 0, ..., N-1 \end{cases} \tag{24}$$

We define $\mathbf{T}^{(i)} = \mathbf{A}^{\mathrm{H}}\mathbf{S}^{(i)}$, where $\mathbf{A}$ is the discrete Fourier transform (DFT) matrix given by $\mathbf{A} = \frac{1}{\sqrt{MK}}[\boldsymbol{\alpha}_1, ..., \boldsymbol{\alpha}_{MK}]^{\mathrm{T}}$, and $\boldsymbol{q}^{(i)} \in \mathbb{C}^{MK}$. The m-th element of $\boldsymbol{q}^{(i)}$ can be expressed as $q_m^{(i)} = \boldsymbol{t}_m^{(i)} \cdot (\boldsymbol{t}_m^{(i)})^{\mathrm{H}}$, where $(\boldsymbol{t}_m^{(i)})$ is the m-th row vector of $\mathbf{T}^{(i)}$. Let $\mathbf{Q} = \mathrm{Diag}\{\boldsymbol{q}^{(i)}\}$, then Equation (24) can be written as:

$$\begin{cases} \min\limits_{\boldsymbol{s}} & \mathrm{Re}(\mathrm{Tr}(\mathbf{S}^{\mathrm{H}}(\mathbf{A}\mathbf{Q}^{(i)}\mathbf{A}^{\mathrm{H}} - \mathbf{S}^{(i)}(\mathbf{S}^{(i)})^{\mathrm{H}})\mathbf{S}^{(i)})) \\ s.t. & |s_n| = 1, n = 0, ..., N-1 \end{cases} \tag{25}$$

It is worth noting that $\mathbf{Q}$ is essentially a spectral power sum matrix that encompasses all bands and Equation (25) is a quadratic function on $\mathbf{S}$. Due to $\mathbf{A}^{\mathrm{H}}\mathbf{A} = \mathbf{I}$, Equation (25) can be formulated as:

$$\begin{cases} \min\limits_{\boldsymbol{s}} & \mathrm{Re}(\mathrm{Tr}(\mathbf{S}^{\mathrm{H}}(\mathbf{A}^{\mathrm{H}}\boldsymbol{\Psi}^{(i)}\mathbf{A})\mathbf{S}^{(i)})) \\ s.t. & |s_n| = 1, n = 0, ..., N-1 \end{cases} \tag{26}$$

where $\boldsymbol{\Psi}^{(i)} = \mathbf{Q}^{(i)} - \mathbf{T}^{(i)}(\mathbf{T}^{(i)})^{\mathrm{H}}$, let $\mathbf{M}^{(i)} = \boldsymbol{\Psi}^{(i)} - q_{\max}^{(i)}\mathbf{I}$, where $q_{\max}^{(i)} = \max\limits_{p}\{q_p^{(i)} : p = 1, ..., MK\}$. Equation (27) can be written as:

$$\begin{cases} \min\limits_{\boldsymbol{s}} & \mathrm{Re}(\mathrm{Tr}(\mathbf{S}^{\mathrm{H}}(\mathbf{A}\mathbf{M}^{(i)}\mathbf{A}^{\mathrm{H}})\mathbf{S}^{(i)})) \\ s.t. & |s_n| = 1, n = 0, ..., N-1 \end{cases} \tag{27}$$

By defining $\mathbf{Z}^{(i)} = -\mathbf{A}\mathbf{M}^{(i)}\mathbf{T}^{(i)}$, when we only consider the unimodular constraint, the majorized problem of Equation (27) can be simplified as follows:

$$\begin{cases} \min\limits_{\boldsymbol{s}} & \|\mathbf{S} - \mathbf{Z}^{(i)}\|_{\mathrm{Fro}} \\ s.t. & |s_n| = 1, n = 0, ..., N-1 \end{cases} \tag{28}$$

$\|\cdot\|_{\mathrm{Fro}}$ in (28) represents the Frobenius norm operator. It is easy to see that the problem given in Equation (27) has a closed-form solution, which is given by:

$$\mathbf{S} = e^{j\arg(\mathbf{Z}^{(i)})} \tag{29}$$

It is important to note that the solution of (29) considers only unimodular constraints, specifically $|s_n| = 1, n = 0, ..., N-1$, and the solution of the similarity constraint and the spectral constraints in (19) will be presented in Section 4.2. The overall algorithm is summarized in Algorithm 1. While local optimization algorithms typically ensure a monotonic behavior of the optimization objective and eventual convergence through the optimization process, the monotonic minimizer for probability of intercept (MPI) formulation itself provides useful insights, as demonstrated in Appendix C.

Algorithm 1 MPI-Monotonic minimizer for probability of intercept

Require: the size of $\mathbf{S}$, i.e., MK, P
Set $k = 0$,initialize $\mathbf{S}^{(0)}$
repeat
  $\mathbf{T}^{(i)} = \mathbf{A}^{\mathrm{H}}\mathbf{S}^{(i)}$,$\mathbf{Q}^{(i)} = \mathrm{Diag}(\boldsymbol{q}^{(\mathrm{i})})$
  $\boldsymbol{\Psi}^{(i)} = \mathbf{Q}^{(i)} - \mathbf{T}^{(i)}(\mathbf{T}^{(i)})^{\mathrm{H}}$
  $q_{\max}^{(i)} = \max\limits_{p}\{q_p^{(i)} : p = 1, ..., MK\}$
  $\mathbf{M}^{(i)} = \boldsymbol{\Psi}^{(i)} - q_{\max}^{(i)}\mathbf{I}$
  $\mathbf{Z}^{(i)} = -\mathbf{A}\mathbf{M}^{(i)}\mathbf{T}^{(i)}$
  $\mathbf{S}^{(i)} = e^{j\arg(\mathbf{Z}^{(i)})}$
  $k \longleftarrow k + 1$
until convergence

The sliding window matrix $\mathbf{S}$, defined by Equation (13), can be uniquely obtained from $\boldsymbol{s}$. However, the converse is not true. According to the mapping relation, $\boldsymbol{s}$ can be mapped by several columns of $\mathbf{S}$, with the number of mappings depending on the overlap time of the receiver window. To better extract $\boldsymbol{s}$ from $\mathbf{S}$, waveform extraction approaches are introduced based on the number-first and length-first principles, respectively.

3.1.1. Number-First

In this subsection, we present a sequence extraction approach based on the time-domain circular shift theorem, which yields a sequence characterized by a constant envelope in the time–frequency domain.

Theorem 1. *Let* $\mathbf{S}^*$ *be an optimized sliding window matrix, where* $\boldsymbol{s}_m$ *represents the mth column of* $\mathbf{S}^*$*. Assuming that* $\|\mathbf{A}\boldsymbol{s}_m\|_2^2 \leq \varrho$*, where* ϱ *is a positive number, there exists a unique transformation* $\hat{s}_m(n) = s_m(mod(n, MK))$*. This transformation guarantees that the resulting sliding window matrix* $\hat{\mathbf{S}}_m$ *satisfies the inequality* $\|\mathbf{A}\hat{\mathbf{S}}_m\|_{\text{Fro}}^2 \leq P\varrho$*.*

Proof of Theorem 1. From Equation (13), the sliding window matrix of $\hat{\boldsymbol{s}}_m$ is

$$\hat{\mathbf{S}}_m = \begin{bmatrix} \mathbf{J}_1\hat{\boldsymbol{s}}_m & | & \cdots & | & \mathbf{J}_P\hat{\boldsymbol{s}}_m \end{bmatrix} \tag{30}$$

Let $\hat{\mathbf{U}}_m = \mathbf{A}\hat{\mathbf{S}}_m$ and $\boldsymbol{u}_p^m, p = 1, ..., P$ is the pth colomn of $\hat{\mathbf{U}}_m$. According to the time-domain cyclic shift theorem [50]

$$\|\mathbf{A}\boldsymbol{s}_m\|_2^2 = \|\boldsymbol{u}_p^m\|_2^2 \leq \varrho, p = 1, ..., P \tag{31}$$

$\|\hat{\mathbf{U}}_m\|_{\text{Fro}}^2$ can be expanded as

$$\begin{aligned} \|\hat{\mathbf{U}}_m\|_{\text{Fro}}^2 &= \sum_{p=1}^{P}\sum_{i=1}^{MK} |u_{i,p}^m|^2 \\ &= \sum_{p=1}^{P} \|\boldsymbol{u}_p^m\|_2^2 \\ &= P \cdot \|\boldsymbol{u}_p^m\|_2^2 \leq P \cdot \varrho, p = 1, ..., P \end{aligned} \tag{32}$$

where $u_{i,p}^m$ is the (i, p)th element of $\hat{\mathbf{U}}_m$. Proof is complete. □

From Theorem 1, we can obtain the expression for $\boldsymbol{s}$ from the sliding window matrix $\mathbf{S}$ as follows:

$$\hat{\boldsymbol{s}}_i(n) = \boldsymbol{s}_i(mod(n, MK)), n = 1, ..., N, i = 1, ..., P \tag{33}$$

where $\boldsymbol{s}_i$ denotes the i-th column vector of $\mathbf{S}$. It should be noted that any column in $\mathbf{S}$ is convergent. Therefore, we can obtain at most P distinct $\hat{\boldsymbol{s}}$ from $\mathbf{S}$. However, the cyclic nature of $\hat{\boldsymbol{s}}$ leads to a deterioration in the correlation property. When N is relatively large, this approach is not suitable for constructing the sequence.

3.1.2. Length-First

In this subsection, we introduce a length-first extraction method. As mentioned in the previous section, the number-first extraction approach, while better conforming to (14), is not suitable for constructing long sequences when N is relatively large due to the cyclic nature of the time-domain. In such cases, we can extract $\hat{\boldsymbol{s}}$ as follows:

$$\hat{\boldsymbol{s}} = \text{vec}(\mathbf{S}) \tag{34}$$

Clearly, the $\hat{\boldsymbol{s}}$ extracted in this way has a maximum length of PMK. It is worth mentioning that the sequence obtained by this extraction will be somewhat distorted for $\gamma > 0$. However, due to Theorem 1, the sequence is somewhat robust. For ease of discussion, in this paper, we only consider the length-first extracted method.

3.2. Minimizer Constrained by Similarity Constraint and Spectral Constraint

In this subsection, we provide optimized solutions for similarity constraints and spectral constraints for MPI.

3.2.1. Constrained by Similarity Constraint

The similarity constrain in Equation (16) is equivalent to $\mathrm{Re}(\hat{s}_n^* s_0(n)) \geq 1 - \xi^2/2$ for $n = 1, 2, ..., N$, implying that $\arg(\hat{s}_n) \in [\gamma_n, \gamma_n + \delta]$, where $\gamma_n = \arg(s_0(n)) - \arccos(1 - \xi^2/2)$, $\delta = 2\arccos(1 - \xi^2/2)$. Letting φ_n be the phase of $\hat{s}_n$, the optimal solution φ_n^* can be given as [51]:

$$\varphi_n^* = \begin{cases} \gamma_n + \delta, & if \cos(\varphi_n + \gamma_n + \delta) \geq \cos(\varphi_n + \gamma_n) \\ \gamma_n, & if \cos(\varphi_n + \gamma_n + \delta) < \cos(\varphi_n + \gamma_n) \end{cases} \tag{35}$$

3.2.2. Constrained by Spectral Constraint under Similarity Constraint

As shown in Equation (18), the optimization problem is utilized to enforce similarity constraints and spectral constraints, ensuring that the designed waveforms satisfy these requirements.

For a given $\epsilon > 0$ in (19), we can always find a ρ such that problem (14) can be transformed into the following equivalent problem:

$$\begin{cases} \min\limits_{\mathbf{S}} & \sum_{m=1}^{MK} ((\boldsymbol{\alpha}_m^{\mathrm{H}} \mathbf{S})^{\mathrm{H}} (\boldsymbol{\alpha}_m^{\mathrm{H}} \mathbf{S}))^2 + \rho \sum_{k \in \Omega} (\boldsymbol{\alpha}_k^{\mathrm{H}} \mathbf{S})^{\mathrm{H}} (\boldsymbol{\alpha}_k^{\mathrm{H}} \mathbf{S}) \\ s.t. & |s_n| = 1, n = 0, ..., N-1 \\ & \|\hat{\mathbf{s}} - \boldsymbol{s}_0\|_\infty \leq \xi \end{cases} \tag{36}$$

where Ω is the low-power frequency band. From here, we can follow the derivation of MPI to obtain the spectral-MPI algorithm for problem (26), and (26) can be rewritten as:

$$\begin{cases} \min\limits_{\mathbf{S}} & \mathrm{Re}(\mathrm{Tr}(\mathbf{T}^{\mathrm{H}} (\widehat{\mathbf{Q}}^{(i)} - \mathbf{T}^{(i)} (\mathbf{T}^{(i)})^{\mathrm{H}}) (\mathbf{T}^{(i)})^{\mathrm{H}})) \\ s.t. & |s_n| = 1, n = 0, ..., N-1 \\ & \|\hat{\mathbf{s}} - \boldsymbol{s}_0\|_\infty \leq \xi \end{cases} \tag{37}$$

where $\widehat{\mathbf{Q}}^{(i)} = \mathrm{Diag}\{\hat{\boldsymbol{q}}^{(i)}\}$, and the m-th element of $\hat{\boldsymbol{q}}^{(i)}$ can be rewritten as

$$\hat{q}_m^{(i)} = \begin{cases} \boldsymbol{t}_p^{(i)} (\boldsymbol{t}_p^{(i)})^{\mathrm{H}} + \rho/2, & m \in \Omega \\ \boldsymbol{t}_p^{(i)} (\boldsymbol{t}_p^{(i)})^{\mathrm{H}}, & otherwise. \end{cases} \tag{38}$$

By defining $\hat{q}_{\max}^{(i)} = \max\limits_m \{\hat{q}_m^{(i)} : m = 1, ..., n_0\}$, $\widehat{\mathbf{\Psi}}^{(i)} = \widehat{\mathbf{Q}}^{(i)} - \mathbf{T}^{(i)} (\mathbf{T}^{(i)})^{\mathrm{H}}$ and $\widehat{\mathbf{M}}^{(i)} = \widehat{\mathbf{\Psi}}^{(i)} - \hat{q}_{\max}^{(i)} \mathbf{I}$, the problem can be recast as shown in (28):

$$\begin{cases} \min\limits_{\mathbf{S}} & \mathrm{Re}(\mathrm{Tr}(\mathbf{S}^{\mathrm{H}} (\mathbf{A} \widehat{\mathbf{M}}^{(i)} \mathbf{A}^{\mathrm{H}}) \mathbf{S}^{(i)})) \\ s.t. & |s_n| = 1, n = 0, ..., N-1 \\ & \|\hat{\mathbf{s}} - \boldsymbol{s}_0\|_\infty \leq \xi \end{cases} \tag{39}$$

This problem has the same form as problem (28), for which the similarity constraint solution is shown in Equation (35). Therefore, we can follow the same steps as before to derive the spectral-MPI algorithm, the main steps of which are listed in Algorithm 2.

Algorithm 2 Spectral-MPI

Require: the size of $\mathbf{S}$, i.e., MK, P
1: Set $k = 0$,initialize $\mathbf{S}^{(0)}$
2: **repeat**
3: $\hat{q}_m^{(i)} = \begin{cases} \boldsymbol{t}_p^{(i)}(\boldsymbol{t}_p^{(i)})^{\mathrm{H}} + \rho/2, & m \in \Omega \\ \boldsymbol{t}_p^{(i)}(\boldsymbol{t}_p^{(i)})^{\mathrm{H}}, & otherwise. \end{cases}$
4: $\mathbf{T}^{(i)} = \mathbf{A}^{\mathrm{H}}\mathbf{S}^{(i)}$,$\widehat{\mathbf{Q}}^{(i)} = \mathrm{Diag}\{\hat{\boldsymbol{q}}^{(i)}\}$
5: $\widehat{\mathbf{\Psi}}^{(i)} = \widehat{\mathbf{Q}}^{(i)} - \mathbf{T}^{(\mathrm{k})}(\mathbf{T}^{(\mathrm{k})})^{\mathrm{H}}$
6: $\hat{q}_{\max}^{(i)} = \max_m\{\hat{q}_m^{(i)} : m = 1, ..., n_0\}$
7: $\widehat{\mathbf{M}}^{(i)} = \widehat{\mathbf{\Psi}}^{(i)} - \hat{q}_{\max}^{(\mathrm{k})}\mathbf{I}$
8: $\widehat{\mathbf{Z}}^{(i)} = -\mathbf{A}\widehat{\mathbf{M}}^{(i)}\mathbf{T}^{(i)}$
9: $\mathbf{S}^{(i)} = e^{j\arg(\widehat{\mathbf{Z}}^{(i)})}$
10: $k \longleftarrow k + 1$
11: **until** convergence

3.3. Computational Complexity of the Minimizer

The computational complexity of each iteration in MPI is primarily dominated by two matrix multiplications involving $\mathbf{A}$, as shown in Algorithm 1. These computations can be easily performed using FFT and IFFT operations. Specifically, in the i-th iteration, the i-th column of $\mathbf{T}^{(i)}$ corresponds to the MK-FFT operation of the i-th column of $\mathbf{S}^{(i)}$, with a computational complexity of $\mathcal{O}(MKP\log(MK))$. The matrix product $\mathbf{T}^{(i)}(\mathbf{T}^{(i)})^{\mathrm{H}}$ needs to be computed only once, and $\mathbf{Q}$ can be obtained from a diagonal vector, with a computational complexity of $\mathcal{O}(MK + P(MK)^2)$. Similarly, the matrix $\mathbf{Z}^{(i)}$ can be obtained by P MK-IFFT operation, with a computational complexity of $\mathcal{O}(MKP\log(MK))$. Additionally, the computational complexity of performing complex angle operations on $\widehat{\mathbf{Z}}^{(i)}$ is denoted by $\mathcal{O}(MKP)$. In summary, the computational complexity of each iteration can be expressed as $\mathcal{O}(2MKP\log(MK) + MK(MKP + P + 1))$. The MPI algorithm exhibits high computational efficiency by using P FFT and IFFT operations, making it suitable for designing long sequences.

3.4. Acceleration Scheme

We also propose an improved version of the MPI algorithm to speed up the convergence process.

The MPI algorithm is derived based on the majorization–minimization principle, and the nature of the majorization functions determines the convergence rate of the algorithm. However, numerical simulations have shown that MPI converges very slowly when N is large. In this subsection, we address this issue and propose an acceleration scheme to improve the convergence speed of the algorithm. The acceleration scheme is called the squared iterative method (SQUAREM), which was originally proposed in [52] to accelerate any EM algorithm. Here, we outline the main steps of SQUAREM and modify it accordingly to address the waveform design problem we encounter.

Let $\mathbb{F}$ denote the fixed-point mapping during the iterations of the proposed MPI algorithm (noting that the mapping varies with the enforced constrains), i.e.,

$$\mathbf{S}^{(i+1)} = \mathbb{F}(\mathbf{S}^{(i)}) \tag{40}$$

Motivated by the Cauchy–Barzilai–Borwein (CBB) method for accelerating the convergence of the classical Cauchy method for solving linear equations, the SQUAREM method iterates as follows:

$$\mathbf{S}^{(i+1)} = e^{j\arg(\mathbf{S}^{(i)} - 2\alpha^{(i)}\mathbf{R}^{(i)} + (\alpha^{(i)})^2\mathbf{V}^{(i)})} \tag{41}$$

where $\mathbf{R}^{(i)} = \mathbb{F}(\mathbf{S}^{(i)}) - \mathbf{S}^{(i)}$, $\mathbf{V}^{(i)} = \mathbb{F}(\mathbb{F}(\mathbf{S}^{(i)})) - \mathbb{F}(\mathbf{S}^{(i)}) - \mathbf{R}^{(i)}$, and $\alpha^{(i)}$ is the step-length in i-th iteration. Follow the step update approach as follows:

$$\alpha^{(i)} = -\frac{\|\mathbf{R}\|_{\text{Fro}}}{\|\mathbf{V}\|_{\text{Fro}}} \tag{42}$$

where $\|\cdot\|_{\text{Fro}}$ is the Frobenius norm. To ensure the descent property, a backtracking strategy is adopted. This strategy repeatedly halves the distance between $\alpha^{(i)}$ and -1 (i.e., $\alpha^{(i)} \longleftarrow (\alpha^{(i)} - 1)/2$) until the descent property is maintained. Monotonicity can be determined by checking whether $\|\mathbf{A}^{\text{H}}\mathbf{S}^{(i+1)}\|_{\text{Fro}} \leq \|\mathbf{A}^{\text{H}}\mathbf{S}^{(i)}\|_{\text{Fro}}$ holds or not. The accelerated MPI based on SQUAREM is summarized in Algorithm 3.

It is worth noting that in each iteration, the acceleration scheme requires the computation of $\mathbf{S}^{(i+1)}$ and $\mathbf{S}^{(i+2)}$, as well as the Frobenius norm and angle operations associated with MKP, which increases the computational complexity of the acceleration scheme. However, the acceleration scheme can significantly reduce the number of iterations, thereby achieving a faster convergence time.

Algorithm 3 Accelerate-MPI

Require: the size of $\mathbf{S}$, i.e., MK, P.
Set $k = 0$,initialize $\mathbf{S}^{(0)}$
repeat
  $\mathbf{R}^{(i)} = \mathbb{F}(\mathbf{S}^{(i)}) - \mathbf{S}^{(i)}$,
  $\mathbf{V}^{(i)} = \mathbb{F}(\mathbb{F}(\mathbf{S}^{(i)})) - \mathbb{F}(\mathbf{S}^{(i)}) - \mathbf{R}^{(i)}$,
  $\alpha^{(i)} = -\frac{\|\mathbf{R}\|_{\text{Fro}}}{\|\mathbf{V}\|_{\text{Fro}}}$
  $\mathbf{S}^{(i+1)} = e^{j\arg(\mathbf{S}^{(i)} - 2\alpha^{(i)}\mathbf{R}^{(i)} + (\alpha^{(i)})^2\mathbf{V}^{(i)})}$
  while $\|\mathbf{A}^{\text{H}}\mathbf{S}^{(i+1)}\|_{\text{Fro}} \leq \|\mathbf{A}^{\text{H}}\mathbf{S}^{(i)}\|_{\text{Fro}}$
    $\alpha^{(i)} \longleftarrow (\alpha^{(i)} - 1)/2$
    $\mathbf{S}^{(i+1)} = e^{j\arg(\mathbf{S}^{(i)} - 2\alpha^{(i)}\mathbf{R}^{(i)} + (\alpha^{(i)})^2\mathbf{V}^{(i)})}$
  end while
  $k \longleftarrow k + 1$
until convergence

4. Numerical Results and Analysis

In this section, we provide several numerical examples to demonstrate the performance of the proposed algorithm. All experiments were performed on a PC with a 2.9 GHz AMD-Ryzen7-4800HS CPU and 24 GB RAM.

4.1. Convergence Performance

We first compared the convergence speed of the MPI algorithm with the accelerated MPI algorithm, measured by the square root of (14), denoted by $\Lambda^{(i)}$. For all algorithms in this experiment, the stopping criterion was set to $|\Lambda^{(i+1)} - \Lambda^{(i)} \leq 10^{-8}|$, and the initial sequence $\{x_n^{(0)}\}_{n=1}^N$ was chosen to be $\{e^{j2\pi\theta_n}\}_{n=1}^N$, where $\{\theta_n\}_{n=1}^N$ are independent random variables uniformly distributed in $[0, 1]$. In the spectrum-MPI of this subsection, the low power frequency band Ω is set to $[0.2, 0.8]$ and $\rho = 1$. To reduce the amount of computation, the sequence extraction approach in this paper is based on the principle of length-first.

Figure 2 shows the convergence properties of the MPI algorithm and the spectral MPI algorithm with their respective acceleration schemes for different parameters. We observe that the proposed MPI and spectral-MPI algorithms always converge monotonically, and the accelerated algorithm is effective in increasing the convergence rate. Additionally, Figure 3 compares the convergence time of the MPI, accelerated MPI, and CAN [53] algorithms with respect to the sequence length N. The results show that the accelerated MPI algorithm has a faster convergence time than the MPI algorithm. Moreover, since the

size of the FFT operation is related to the size of MK, the convergence time of the proposed algorithm does not significantly increase with the sequence length, unlike the case of CAN.

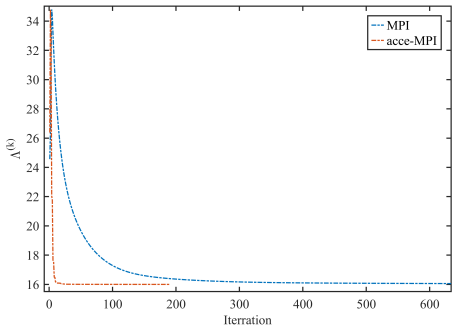

(**a**) $N = 256, M = 8, K = 8$

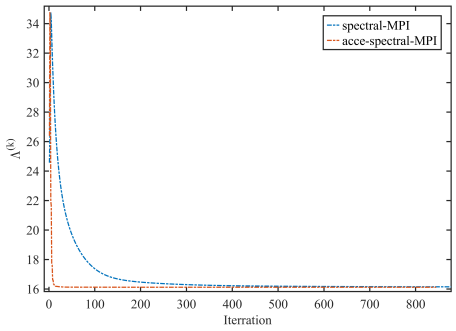

(**b**) $N = 256, M = 8, K = 8$

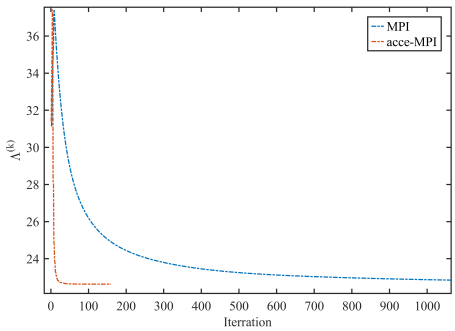

(**c**) $N = 512, M = 8, K = 16$

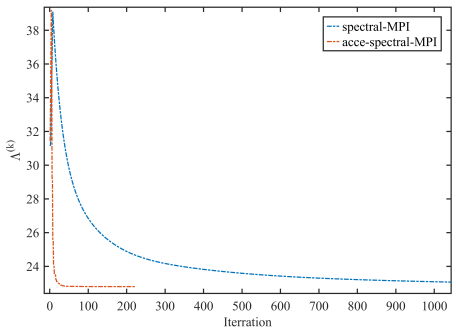

(**d**) $N = 512, M = 8, K = 16$

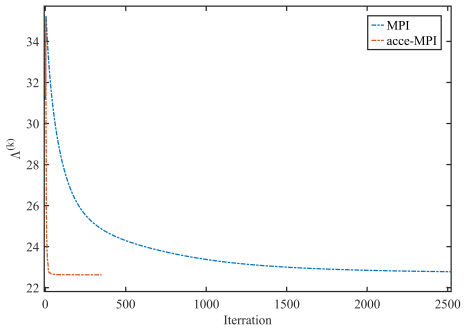

(**e**) $N = 512, M = 16, K = 16$

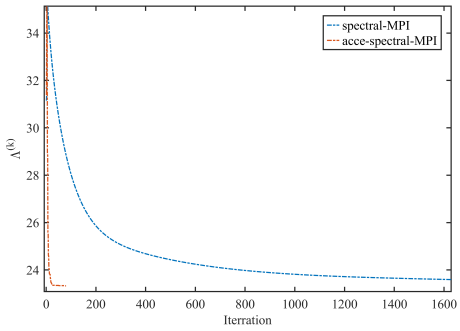

(**f**) $N = 512, M = 16, K = 16$

Figure 2. Comparison of the convergence between MPI and spectral-MPI with different parameters and their respective accelerated versions.

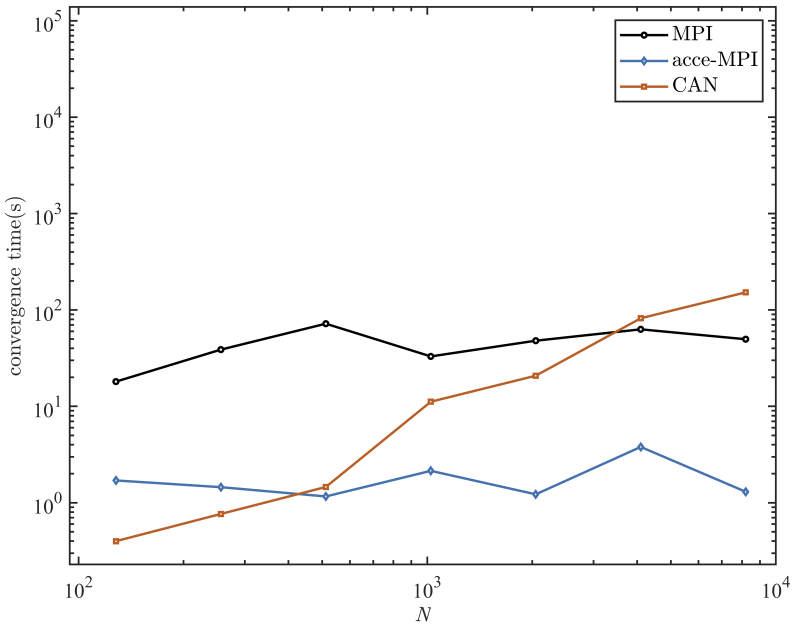

Figure 3. Comparison of the convergence time of the spectral-MPI and accelerate-spectral-MPI.

4.2. LPI Performance

Subsequently, an experiment is conducted to illustrate the superior interference performance of the proposed sequence in comparison to commonly utilized sequences like SIN, LFM, CAN, and Golomb [54]. Among these, SIN and LFM can be respectively defined as a sine signal represented by $\exp(j0.2\pi n)$ and a linear frequency modulated signal represented by $\exp(j0.2\pi n^2/N)$. Assuming a free-space propagation model and neglecting gain and loss, the relationship between the maximum propagation distance r_{max} and the minimum received power p_{smin} can be expressed as [55]:

$$r_{max} = \left(\frac{P_t G_t G_r \lambda^2}{(4\pi)^2 p_{smin}} \right)^{1/2} \tag{43}$$

where P_t, λ, G_t, and G_r represent the transmit power, wavelength, transmit gain, and receive gain, respectively. In this experiment, we only consider the cases where $G_t = 1$ and $G_r = 1$. On one hand, $P_t = 10^2$ watts and $\lambda = 0.1$ meters. The sequence is parameterized by $N = 512, M = 16, K = 16$. The minimum output power p_{omin} after processing with the FFT filter bank-based summation detector can be represented as $p_{omin} = p_{smin} \cdot \frac{\max\limits_m \sum_{p=1}^{P} (\mathbf{C}_m^{\mathrm{H}} \mathbf{W} \mathbf{J}_p \boldsymbol{s})^{\mathrm{H}} (\mathbf{C}_m^{\mathrm{H}} \mathbf{W} \mathbf{J}_p \boldsymbol{s})}{PK}$.

Figure 4 compares the intercept distances between common sequences and the proposed sequence for $p_{smin} \in [-90, -70]$ dBm and ES system setting: $M = 8, K = 16$. In this configuration, if $\frac{\max\limits_m \sum_{p=1}^{P} (\mathbf{C}_m^{\mathrm{H}} \mathbf{W} \mathbf{J}_p \boldsymbol{s})^{\mathrm{H}} (\mathbf{C}_m^{\mathrm{H}} \mathbf{W} \mathbf{J}_p \boldsymbol{s})}{PK} = 1$, the theoretical lower bound is computed. Obviously, the proposed sequences have a smaller maximum propagation distance than the normal sequence under the same p_{smin}, especially for SIN with LFM sequences. Moreover, the proposed sequence almost reaches the theoretical lower bound.

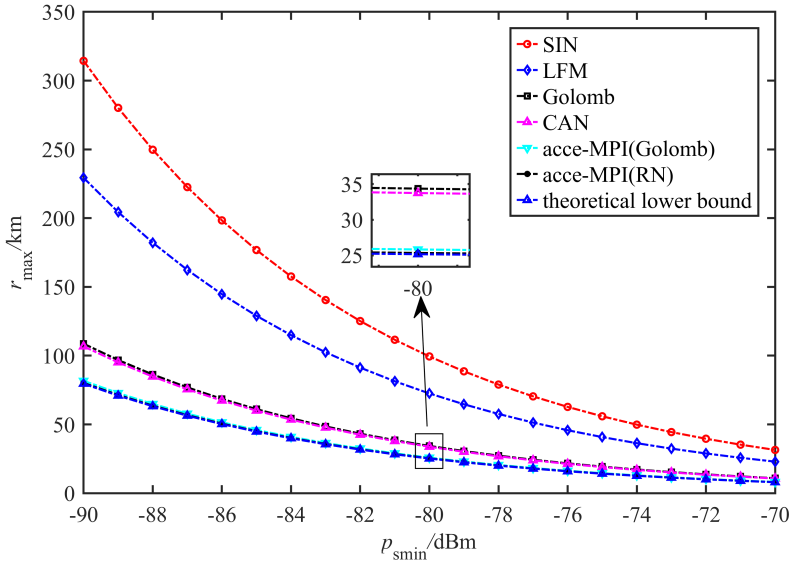

Figure 4. Comparison of the maximum propagation distance of common sequence and accelerated-MPI initialized by different sequences.

Figure 5 compares the maximum intercept distance of the proposed waveform for a minimum received power p_{smin} of -80 dBm and window lengths MK ranging from 80 to 256. The results demonstrate that the proposed algorithm does not require prior knowledge of the receiver window length MK and maintains a low interception property across different window lengths.

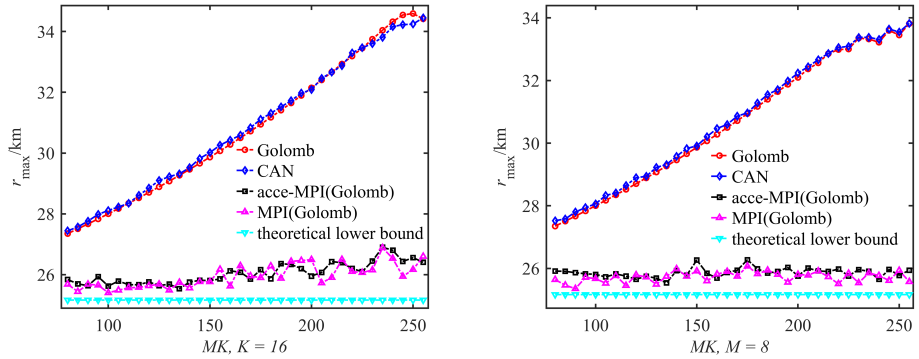

(**a**) Changing the channel number M (**b**) Changing the FFT size K

Figure 5. Comparison of the maximum propagation distance between normal waveforms and accelerated-MPI with different MK.

4.3. Autocorrelation Performance

To investigate the degree to which the similarity constraint improves the autocorrelation properties of the sequence, we conducted an experiment to evaluate the merit factor (MF) under a different ξ. The MF is defined as the ratio of the central lobe energy to the total energy of all other lobes, as proposed by Golay in 1972 [56].

$$\mathrm{MF} = \frac{|r_0|^2}{2\sum_{k=1}^{k=N-1}|r_k|^2} \tag{44}$$

where $\boldsymbol{r}_k$ denotes aperiodic autocorrelations which can be defined as:

$$r_k = \sum_{n=1}^{N-k} x_n x_{n+k}^* = r_{-k}^*, k = 0, ..., N-1 \tag{45}$$

The accelerated-MPI algorithm initialized by Golomb or random (RN) sequence are applied to the following lengths: $N = 2^7, 2^8, 2^9, 2^{10}, 2^{11}, 2^{12}$, with $\xi = 0.01$. We chose the CAN sequence with superior MF properties as the reference sequence. The MF of the resulting sequences is shown in Figure 6. We observe that the MF of the proposed algorithm is almost independent of the sequence length. Figure 7 compares the MF of the accelerated-MPI initialized by Golomb and RN, respectively, versus ξ from 0 to 1, and the proposed sequence is parameterized by $N = 512, M = 8, K = 16$. The results demonstrate that the similarity constraint can improve certain properties as ξ increases, which increases the flexibility of the design.

In addition, we considered the design of spectral constraints with low spectral power in frequency bands $[0, 0.2) \bigcup (0.3, 0.5) \bigcup (0.8, 1]$. Figure 8 shows the time–frequency energy flow of the output sequence generated by spectral-MPI when initialized with a Golomb sequence and $\rho = 1$. To observe the change in time–frequency energy more intuitively due to spectral constraints, Figure 9 shows the time–frequency energy flow without spectral constraints. We observe that the power in the pre-specified frequency bands has been suppressed, and the time–frequency flow is similar to the constant-envelope smooth.

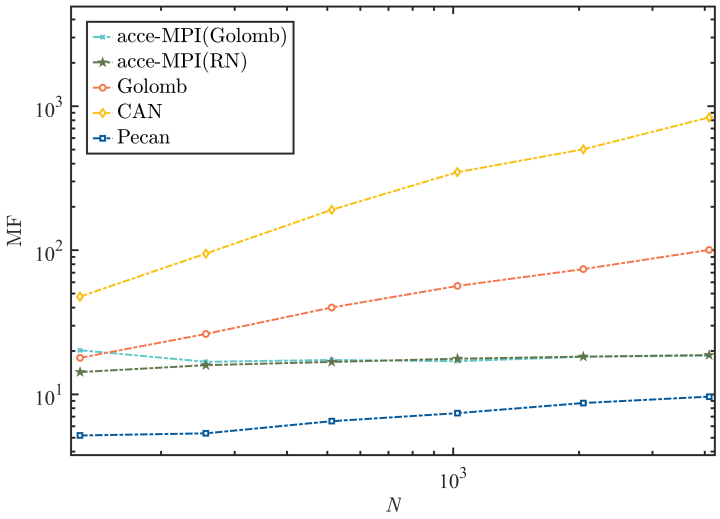

Figure 6. Comparison of the merit factor of common sequences and accelerated-MPI initialized by different sequences.

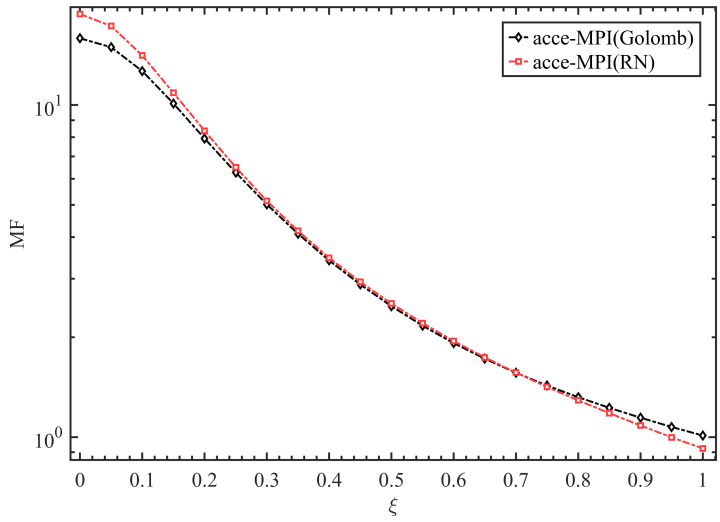

Figure 7. Comparison of the merit factor of accelerated-MPI initialized by different sequences versus ξ.

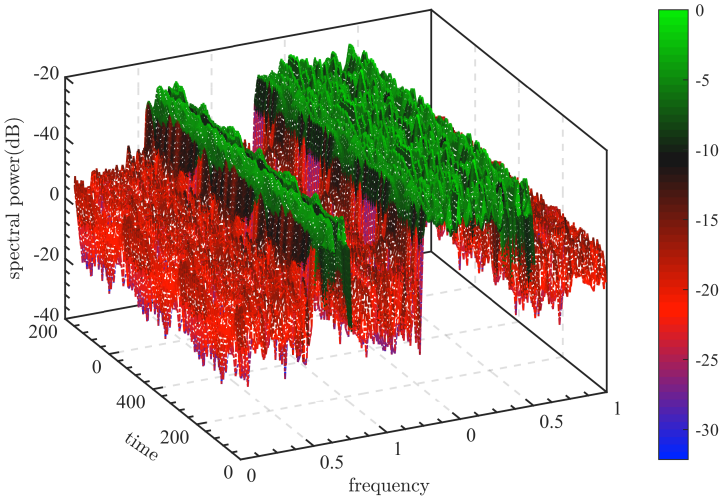

Figure 8. Time–frequency energy flow of spectral-MPI with low spectral power in frequency bands $[0, 0.2) \bigcup (0.3, 0.5) \bigcup (0.8, 1]$.

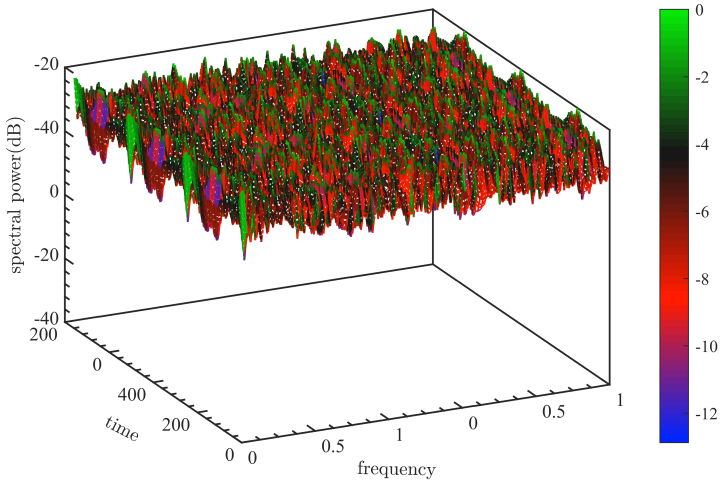

Figure 9. Time–frequency energy flow of spectral-MPI with low spectral power in frequency bands $[0, 1]$.

5. Conclusions

We have introduced the MPI algorithm, an efficient method for minimizing the probability of intercept. This algorithm is derived from the general quadratic optimization framework. In scenarios involving spectral and similarity constraints, we also developed the spectral-MPI algorithm to achieve enhanced properties within the same framework as MPI. Additionally, we have explored acceleration schemes to expedite the MPI algorithm. Numerical results demonstrate that, when applied to FFT filter bank-based summation detectors, the proposed MPI algorithm can generate sequences with a lower probability of intercept compared to common sequences. Moreover, it can be utilized to design sequences with suppressed spectral power in arbitrary frequency bands. Importantly, all of the proposed algorithms can be efficiently implemented using FFT and have demonstrated computational efficiency in practical applications.

Author Contributions: Conceptualization, methodology, software, and writing—original draft preparation, Q.L.; supervision, F.G.; software and validation, K.X.; writing—review and editing, Z.L.; funding acquisition, W.H. All authors have read and agreed to the published version of the manuscript.

Funding: This work was supported in part by the National Natural Science Foundation of China under Grant 62101570 and in part by the National Natural Science Foundation of China under Grant 61901494.

Data Availability Statement: The original contributions presented in this study are included in the article, whilst further inquiries can be directed to the corresponding author.

Conflicts of Interest: The authors declare no conflicts of interest.

Appendix A

Proof of sufficiency of (7). To prove that (8) is a sufficient condition for (7), we need to prove

$$\max_{m,p} \left(\boldsymbol{C}_m^{\mathrm{H}}\mathbf{H}\boldsymbol{J}_p\boldsymbol{r}\right)^{\mathrm{H}}\left(\boldsymbol{C}_m^{\mathrm{H}}\mathbf{H}\boldsymbol{J}_p\boldsymbol{r}\right) \geq \|\boldsymbol{\kappa}\|_\infty \tag{A1}$$

Assuming that there exist m_0 and p_0 such that

$$\begin{aligned}&\max_{m,p} \left(\boldsymbol{C}_m^{\mathrm{H}}\mathbf{H}\boldsymbol{J}_p\boldsymbol{r}\right)^{\mathrm{H}}\left(\boldsymbol{C}_m^{\mathrm{H}}\mathbf{H}\boldsymbol{J}_p\boldsymbol{r}\right)\\ &= \left(\boldsymbol{C}_{m_0}^{\mathrm{H}}\mathbf{H}\boldsymbol{J}_{p_0}\boldsymbol{r}\right)^{\mathrm{H}}\left(\boldsymbol{C}_{m_0}^{\mathrm{H}}\mathbf{H}\boldsymbol{J}_{p_0}\boldsymbol{r}\right)\end{aligned} \tag{A2}$$

When $P = 1$, it is obvious that

$$\left(\boldsymbol{C}_{m_0}^{\mathrm{H}}\mathbf{H}\boldsymbol{J}_{p_0}\boldsymbol{r}\right)^{\mathrm{H}}\left(\boldsymbol{C}_{m_0}^{\mathrm{H}}\mathbf{H}\boldsymbol{J}_{p_0}\boldsymbol{r}\right) \equiv \|\boldsymbol{\kappa}\|_\infty \tag{A3}$$

When $P > 1$, assuming there exists m_1 such that

$$\|\boldsymbol{\kappa}\|_\infty = \frac{1}{P}\sum_{p=1}^{P}\left(\boldsymbol{C}_{m_1}^{\mathrm{H}}\mathbf{H}\boldsymbol{J}_p\boldsymbol{r}\right)^{\mathrm{H}}\left(\boldsymbol{C}_{m_1}^{\mathrm{H}}\mathbf{H}\boldsymbol{J}_p\boldsymbol{r}\right) \tag{A4}$$

Let $p = p_1$ be the maximal term in the summation on the right-hand side of (A4), i.e.,

$$\begin{aligned}&\left(\boldsymbol{C}_{m_1}^{\mathrm{H}}\mathbf{H}\boldsymbol{J}_{p_1}\boldsymbol{r}\right)^{\mathrm{H}}\left(\boldsymbol{C}_{m_1}^{\mathrm{H}}\mathbf{H}\boldsymbol{J}_{p_1}\boldsymbol{r}\right)\\ &\geq \left(\boldsymbol{C}_{m_1}^{\mathrm{H}}\mathbf{H}\boldsymbol{J}_p\boldsymbol{r}\right)^{\mathrm{H}}\left(\boldsymbol{C}_{m_1}^{\mathrm{H}}\mathbf{H}\boldsymbol{J}_p\boldsymbol{r}\right), \forall p \in [1, P]\end{aligned} \tag{A5}$$

Therefore, we have:

$$\begin{aligned}&\left(\boldsymbol{C}_{m_1}^{\mathrm{H}}\mathbf{H}\boldsymbol{J}_{p_1}\boldsymbol{r}\right)^{\mathrm{H}}\left(\boldsymbol{C}_{m_1}^{\mathrm{H}}\mathbf{H}\boldsymbol{J}_{p_1}\boldsymbol{r}\right)\\ &\geq \frac{1}{P}\sum_{p=1}^{P}\left(\boldsymbol{C}_{m_1}^{\mathrm{H}}\mathbf{H}\boldsymbol{J}_p\boldsymbol{r}\right)^{\mathrm{H}}\left(\boldsymbol{C}_{m_1}^{\mathrm{H}}\mathbf{H}\boldsymbol{J}_p\boldsymbol{r}\right)\\ &= \|\boldsymbol{\kappa}\|_\infty\end{aligned}$$

According to the definition,

$$\begin{aligned}&\left(\boldsymbol{C}_{m_0}^{\mathrm{H}}\mathbf{H}\boldsymbol{J}_{p_0}\boldsymbol{r}\right)^{\mathrm{H}}\left(\boldsymbol{C}_{m_0}^{\mathrm{H}}\mathbf{H}\boldsymbol{J}_{p_0}\boldsymbol{r}\right)\\ &\geq \left(\boldsymbol{C}_{m_0}^{\mathrm{H}}\mathbf{H}\boldsymbol{J}_{p_0}\boldsymbol{r}\right)^{\mathrm{H}}\left(\boldsymbol{C}_{m_0}^{\mathrm{H}}\mathbf{H}\boldsymbol{J}_{p_0}\boldsymbol{r}\right)\\ &\geq \|\boldsymbol{\kappa}\|_\infty\end{aligned}$$

This proves that (8) is a sufficient condition for (7). The proof is complete. □

Appendix B

Proof of upper and lower bounds for $\mathrm{vec}(\mathbf{X})^{\mathrm{H}} \cdot \mathrm{vec}(\mathbf{X})$**.** The matrix $\mathbf{S}$ can be represented as:

$$\mathbf{S} = \begin{bmatrix} s_1 & s_{L+1} & \cdots & s_{(P-1)L+1} \\ s_2 & s_{L+2} & \cdots & s_{(P-1)L+2} \\ \vdots & \vdots & \ddots & \vdots \\ s_{MK} & s_{L+MK} & \cdots & s_{(P-1)L+MK} \end{bmatrix} \tag{A6}$$

Since $\mathbf{X} = \mathbf{S}\mathbf{S}^{\mathrm{H}}$, the elements of $\mathbf{X}$, denoted by x_{ij}, can be expressed as:

$$x_{ij} = \sum_{p=1}^{P} s^{*}_{i+(p-1)L} s_{j+(p-1)L} \tag{A7}$$

Given that $\boldsymbol{s}^{\mathrm{H}}\boldsymbol{e}_n^{\mathrm{H}}\boldsymbol{e}_n\boldsymbol{s} = 1$, for $n = 0, ..., N-1$, we can express $\mathrm{vec}(\mathbf{X})^{\mathrm{H}} \cdot \mathrm{vec}(\mathbf{X})$ as:

$$\begin{aligned} \mathrm{vec}(\mathbf{X})^{\mathrm{H}} \cdot \mathrm{vec}(\mathbf{X}) &= \sum_{i=1}^{MK}\sum_{j=1}^{MK}\left|\sum_{p=1}^{P} s^{*}_{p+(i-1)L} s_{p+(j-1)L}\right|^2 \\ &= \sum_{i=1}^{MK}\sum_{j=1\, j\neq i}^{MK}\left|\widetilde{r}_{i,j}\right|^2 + MKP^2 \\ &= \sum_{i=1}^{MK}\sum_{j=1\, j\neq i}^{MK}\left|\boldsymbol{s}_i^{\mathrm{H}} \cdot \boldsymbol{s}_j\right|^2 + MKP^2 \end{aligned} \tag{A8}$$

where $\widetilde{r}_{i,j}$ is the inner product of the vectors of the i-th and j-th windows. When $\forall i, j, \boldsymbol{s}_i^{\mathrm{H}} \cdot \boldsymbol{s}_j = 0$, we have $\mathrm{vec}(\mathbf{X})^{\mathrm{H}} \cdot \mathrm{vec}(\mathbf{X}) = MKP^2$. When $\forall i, j, \boldsymbol{s}_i^{\mathrm{H}} \cdot \boldsymbol{s}_j = P$, we have $\mathrm{vec}(\mathbf{X})^{\mathrm{H}} \cdot \mathrm{vec}(\mathbf{X}) = MK^2P^2$. Thus, we can conclude that:

$$MKP^2 \leq \mathrm{vec}(\mathbf{X})^{\mathrm{H}} \cdot \mathrm{vec}(\mathbf{X}) \leq (MK)^2P^2 \tag{A9}$$

The proof is complete. □

Appendix C

Proof of convergence of the MPI algorithm. $\mathbf{S}^{(i+1)}$ can be expressed as from (30):

$$\mathbf{R}\mathbf{S}^{(i)} = \left[\mathbf{R}\boldsymbol{s}_1^{(i)} \quad | \quad \cdots \quad | \quad \mathbf{R}\boldsymbol{s}_P^{(i)}\right] \tag{A10}$$

where $\mathbf{R} = -\mathbf{A}\mathbf{M}^{(i)}\mathbf{A}^{\mathrm{H}}$ and $\boldsymbol{s}_p^{(i)}$ is the pth column of $\mathbf{S}^{(i)}$. It is easy to know that $\mathbf{R}$ is a positive definite. The monotonicity of the MPI algorithm requires proof of the following equation:

$$\sum_{p=1}^{P}(\boldsymbol{s}_p^{(i+1)})^{\mathrm{H}}\mathbf{R}\boldsymbol{s}_p^{(i+1)} - \sum_{p=1}^{P}(\boldsymbol{s}_p^{(i+1)})^{\mathrm{H}}\mathbf{R}\boldsymbol{s}_p^{(i+1)} \geq 0 \tag{A11}$$

Note that

$$\begin{aligned} &\|\mathbf{S}^{(i+1)} - \mathbf{R}\mathbf{S}^{(i)}\|_{\mathrm{Fro}}^2 \\ =&\sum_{p=1}^{P}\|\boldsymbol{s}_p^{(i+1)} - \mathbf{R}\boldsymbol{s}_p^{(i)}\|_2^2 \end{aligned} \tag{A12}$$

Expanding each term in (A12), we have

$$\begin{aligned} &\sum_{p=1}^{P}\|\boldsymbol{s}_p^{(i+1)} - \mathbf{R}\boldsymbol{s}_p^{(i)}\|_2^2 \\ =&\mathrm{const} - \sum_{p=1}^{P} 2\mathrm{Re}((\boldsymbol{s}_p^{(i+1)})^{\mathrm{H}}\mathbf{R}\boldsymbol{s}^{(i)}) \end{aligned} \tag{A13}$$

For each p, $\boldsymbol{s}_p^{(i+1)}$ is equivalently the maximizer of the criterion $\mathrm{Re}((\boldsymbol{s}_p^{(i+1)})^{\mathrm{H}}\mathbf{R}\boldsymbol{s}^{(i)})$. Moreover, if $\boldsymbol{s}_p^{(i+1)} \neq \boldsymbol{s}_p^{(i)}$, clearly, we have

$$\begin{aligned}\sum_{p=1}^{P}(\boldsymbol{s}_m^{(i+1)})^{\mathrm{H}}\boldsymbol{R}\boldsymbol{s}^{(i+1)} &> \sum_{p=1}^{P}2\mathrm{Re}((\boldsymbol{s}_p^{(i+1)})^{\mathrm{H}}\mathbf{R}\boldsymbol{s}^{(i)}) - \sum_{p=1}^{P}(\boldsymbol{s}_m^{(i)})^{\mathrm{H}}\boldsymbol{R}\boldsymbol{s}^{(i)} \\ &> \sum_{p=1}^{P}(\boldsymbol{s}_m^{(i)})^{\mathrm{H}}\boldsymbol{R}\boldsymbol{s}^{(i)}\end{aligned} \tag{A14}$$

as $\mathrm{Re}((\boldsymbol{s}_p^{(i+1)})^{\mathrm{H}}\mathbf{R}\boldsymbol{s}^{(i)}) > (\boldsymbol{s}_m^{(i)})^{\mathrm{H}}\boldsymbol{R}\boldsymbol{s}^{(i)}, p = 1, ..., P$. The proof is complete. □

References

1. Hu, X.; Yang, J.; Meng, C.; Xu, Y.; Xie, Y. Analysis of Radar Survival Probability against Front Door Coupling Attack Based on Beam Pattern. In Proceedings of the 2023 3rd International Conference on Neural Networks, Information and Communication Engineering (NNICE), Guangzhou, China, 24–26 February 2023; pp. 122–126.
2. Bang, J.H.; Park, H.D.; Lee, W.; Kim, D.; Kim, H.N. Accurate Estimation of LPI Radar Pulse Train Parameters via Change Point Detection. *IEEE Access* **2023**, *11*, 12796–12807. [CrossRef]
3. Shi, C.; Wang, F.; Sellathurai, M.; Zhou, J.; Salous, S. Low Probability of Intercept-Based Optimal Power Allocation Scheme for an Integrated Multistatic Radar and Communication System. *IEEE Syst. J.* **2020**, *14*, 983–994. 2931754. [CrossRef]
4. Glenn, A. Low probability of intercept. *IEEE Commun. Mag.* **1983**, *21*, 26–33. [CrossRef]
5. Pace, P.E.; Griffiths, H.D. Detecting and Classifying Low Probability of Intercept Radar – Second Edition. *Aeronaut. J.* **2011**, *115*, 389. [CrossRef]
6. Grossi, E.; Taremizadeh, H.; Venturino, L. Radar Target Detection and Localization Aided by an Active Reconfigurable Intelligent Surface. *IEEE Signal Process. Lett.* **2023**, *30*, 903–907. [CrossRef]
7. Li, X.; Cai, Z. Deep Learning and Time-Frequency Analysis Based Automatic Low Probability of Intercept Radar Waveform Recognition Method. In Proceedings of the 2023 IEEE 23rd International Conference on Communication Technology (ICCT), Wuxi, China, 20–22 October 2023; pp. 291–296.
8. Jia, J.; Han, Z.; Liu, L. Review on Low Intercept Radar Signal Design Technology. In Proceedings of the 2022 IEEE 4th International Conference on Power, Intelligent Computing and Systems (ICPICS), Shenyang, China, 29–31 July 2022; pp. 434–437.
9. Yang, H.; Chen, J. Design of Costas/PSK Continuous Wave LPI Radar Signal. *Int. J. Electron.* **2017**, *104*, 404–415. [CrossRef]
10. Tao, W.; Kaili, J.; Jingyi, L.; Tingting, J.; Bin, T. Research on LPI radar signal detection and parameter estimation technology. *J. Syst. Eng. Electron.* **2021**, *32*, 566–572. [CrossRef]
11. Xie, M.; Yi, W.; Kong, L.; Kirubarajan, T. Receive-Beam Resource Allocation for Multiple Target Tracking with Distributed MIMO Radars. *IEEE Trans. Aerosp. Electron. Syst.* **2018**, *54*, 2421–2436. [CrossRef]
12. Shi, Y.; An, K.; Li, Y. Index Modulation Based Frequency Hopping: Anti-Jamming Design and Analysis. *IEEE Trans. Veh. Technol.* **2021**, *70*, 6930–6942. [CrossRef]
13. Nowak, M.J.; Zhang, Z.; LoMonte, L.; Wicks, M.; Wu, Z. Mixed-Modulated Linear Frequency Modulated Radar-Communications. *IET Radar Sonar Navig.* **2017**, *11*, 313–320. [CrossRef]
14. Alexander, D.B.; Narayanan, R.M.; Himed, B. Analysis of Sparse Co-Prime Sensing Array Performance Using Wideband Noise Signals. In Proceedings of the 2017 51st Asilomar Conference on Signals, Systems, and Computers, Pacific Grove, CA, USA, 29 October–1 November 2017; pp. 1147–1151.
15. Qiongdan, H.; Yong, L.; Yaoping, Z.; Yinjuan, F. Design and Characteristic Analysis of Multicarrier Chaotic Phase Coded Radar Pulse Train Signal. *Int. J. Antennas Propag.* **2014**, *2014*, 724294.
16. Chen, K.; Zhang, J.; Chen, S.; Zhang, S.; Zhao, H. Recognition and Estimation for Frequency-Modulated Continuous-Wave Radars in Unknown and Complex Spectrum Environments. *IEEE Trans. Aerosp. Electron. Syst.* **2023**, *59*, 6098–6111. [CrossRef]
17. Chen, K.; Wang, L.; Zhang, J.; Chen, S.; Zhang, S. Semantic Learning for Analysis of Overlapping LPI Radar Signals. *IEEE Trans. Instrum. Meas.* **2023**, *72*, 8501615. [CrossRef]
18. Liu, X.; Zhang, T.; Yu, X.; Shi, Q.; Cui, G.; Kong, L. LPI waveform design for radar system against cyclostationary analysis intercept processing. *Signal Process.* **2022**, *201*, 108681. [CrossRef]
19. Schrick, G.; Wiley, R.G. Interception of LPI radar signals. In Proceedings of the IEEE International Conference on Radar, Arlington, VA, USA, 7–10 May 1990; pp. 108–111. [CrossRef]
20. Luo, M.; Zhong, T.; Li, M.; Li, X.; Li, Z.; Wu, J.; Yang, J. Low Probability of Intercept Waveform Optimization Method for Sar Imaging. In Proceedings of the 2021 IEEE International Geoscience and Remote Sensing Symposium IGARSS, Brussels, Belgium, 11–16 July 2021; pp. 3963–3966. [CrossRef]
21. Liu, S.; Cao, Y.; Yeo, T.S.; Wang, F.; Han, J. Range Sidelobe Suppression for Randomized Stepped-Frequency Chirp Radar. *IEEE Trans. Aerosp. Electron. Syst.* **2021**, *57*, 3874–3885. [CrossRef]

22. Liu, S.; Cao, Y.; Yeo, T.S.; Wu, W.; Liu, Y. Adaptive Clutter Suppression in Randomized Stepped-Frequency Radar. *IEEE Trans. Aerosp. Electron. Syst.* **2021**, *57*, 1317–1333. [CrossRef]
23. Hao, X.; Feng, Z.; Yang, S.; Wang, M.; Jiao, L. Automatic Modulation Classification via Meta-Learning. *IEEE Internet Things J.* **2023**, *10*, 12276–12292. [CrossRef]
24. Wang, L.; Wang, W.Q.; Guan, H.; Zhang, S. LPI Property of FDA Transmitted Signal. *IEEE Trans. Aerosp. Electron. Syst.* **2021**, *57*, 3905–3915. [CrossRef]
25. Gong, P.; Zhang, Z.; Wu, Y.; Wang, W.Q. Joint Design of Transmit Waveform and Receive Beamforming for LPI FDA-MIMO Radar. *IEEE Signal Process. Lett.* **2022**, *29*, 1938–1942. [CrossRef]
26. Jin, Y.; Duan, P.; Ji, H. Parameter Estimation of LFM Signals Based on Scaled Ambiguity Function. *Circuits Syst. Signal Process.* **2016**, *35*, 4445–4462. [CrossRef]
27. Hamschin, B.M.; Ferguson, J.D.; Grabbe, M.T. Interception of Multiple Low-Power Linear Frequency Modulated Continuous Wave Signals. *IEEE Trans. Aerosp. Electron. Syst.* **2017**, *53*, 789–804. [CrossRef]
28. Alphonse, S.; Williamson, G.A. On Estimating Nonlinear Frequency Modulated Radar Signals in Low SNR Environments. *IEEE Trans. Aerosp. Electron. Syst.* **2021**, *57*, 1793–1802. [CrossRef]
29. Chen, J.; Wang, J.; Zhang, Y.; Wang, F.; Zhou, J. Spatial Information-Theoretic Optimal LPI Radar Waveform Design. *Entropy* **2022**, *24*, 1515. [CrossRef] [PubMed]
30. Chen, J.; Wang, F.; Zhou, J. Information-Theoretic Optimal Radar Waveform Selection with Multi-Sensor Cooperation for LPI Purpose. *IEEE Access* **2022**, *10*, 113649–113661. [CrossRef]
31. Williams, E.C.; Bridges, C.P.; Bowyer, D.J.M. Nowhere to hide? Passive, non-cooperative maritime surveillance from a nanosat. In Proceedings of the 2018 IEEE Aerospace Conference, Big Sky, MT, USA, 3–10 March 2018; pp. 1–10. [CrossRef]
32. Ellis, P.; Rheeden, D.V.; Dowla, F. Use of Doppler and Doppler Rate for RF Geolocation Using a Single LEO Satellite. *IEEE Access* **2020**, *8*, 12907–12920. [CrossRef]
33. Kim, I.; Park, K.H.; Song, M.K.; Song, H.Y.; Lee, J.Y. Design of LPI signals using optimal families of perfect polyphase sequences. In Proceedings of the 2016 International Symposium on Information Theory and Its Applications (ISITA), Monterey, CA, USA, 30 October–2 November 2016; pp. 261–264.
34. Warnke, L.; Correll, B.; Swanson, C.N. The Density of Costas Arrays Decays Exponentially. *IEEE Trans. Inf. Theory* **2023**, *69*, 575–581. [CrossRef]
35. Gong, P.; Xu, K.; Wu, Y.; Zhang, J.; So, H.C. Optimization of LPI-FDA-MIMO Radar and MIMO Communication for Spectrum Coexistence. *IEEE Wirel. Commun. Lett.* **2023**, *12*, 1076–1080. [CrossRef]
36. Su, Y.; Cheng, T.; He, Z. LPI-Constrained Collaborative Transmit Beampattern Optimization and Resource Allocation for Maneuvering Targets Tracking in Colocated MIMO Radar Network. *Signal Process.* **2023**, *207*, 108935. [CrossRef]
37. Antonik, P.; Wicks, M.C.; Griffiths, H.D.; Baker, C.J. Frequency diverse array radars. In Proceedings of the 2006 IEEE Conference on Radar, Verona, NY, USA, 24–27 April 2006; p. 3. [CrossRef]
38. Pandit, S.; Singh, G. Spectrum Sensing in Cognitive Radio Networks: Potential Challenges and Future Perspective. In *Spectrum Sharing in Cognitive Radio Networks: Medium Access Control Protocol Based Approach*; Springer International Publishing: Cham, Switzerland, 2017; pp. 35–75. [CrossRef]
39. Aubry, A.; Carotenuto, V.; De Maio, A.; Govoni, M.A.; Farina, A. Experimental Analysis of Block-Sparsity-Based Spectrum Sensing Techniques for Cognitive Radar. *IEEE Trans. Aerosp. Electron. Syst.* **2021**, *57*, 355–370. [CrossRef]
40. Kuzdeba, S.; Radlbeck, A.; Anderson, M. Performance Metrics for Cognitive Electronic Warfare - Electronic Support Measures. In Proceedings of the MILCOM 2018—2018 IEEE Military Communications Conference (MILCOM), Los Angeles, CA, USA, 29–31 October 2018; pp. 1–9. [CrossRef]
41. Mariani, A.; Giorgetti, A.; Chiani, M. Energy Detector Design for Cognitive Radio Applications. In Proceedings of the 2010 International Waveform Diversity and Design Conference, Niagara Falls, ON, Canada, 8–13 August 2010; pp. 53–57.
42. Saarnisaari, H.; Vartiainen, J. Signal detection with spectrum windows. *Heliyon* **2022**, *8*, e10054. [CrossRef]
43. Wang, J.; Xie, Y.; Li, B.; Yang, C.; Hu, S. The Reconfigurable Pipelined Variable-Point FFT Processor Design. In Proceedings of the 2019 IEEE International Conference on Signal, Information and Data Processing (ICSIDP), Chongqing, China, 11–13 December 2019; pp. 1–4.
44. Soltanalian, M.; Tang, B.; Li, J.; Stoica, P. Joint Design of the Receive Filter and Transmit Sequence for Active Sensing. *IEEE Signal Process. Lett.* **2013**, *20*, 423–426. [CrossRef]
45. Wang, S.; Inkol, R.; Rajan, S.; Patenaude, F. On the Performance Gain of the FFT Filter-Bank-Based Summation and Majority CFAR Detectors. *IEEE Trans. Instrum. Meas.* **2009**, *58*, 1778–1788. [CrossRef]
46. Tang, B.; Li, J.; Liang, J. Alternating direction method of multipliers for radar waveform design in spectrally crowded environments. *Signal Process.* **2018**, *142*, 398–402. [CrossRef]
47. Aubry, A.; DeMaio, A.; Farina, A.; Wicks, M. Knowledge-Aided (Potentially Cognitive) Transmit Signal and Receive Filter Design in Signal-Dependent Clutter. *IEEE Trans. Aerosp. Electron. Syst.* **2013**, *49*, 93–117. [CrossRef]
48. Soltanalian, M.; Stoica, P. Designing Unimodular Codes Via Quadratic Optimization. *IEEE Trans. Signal Process.* **2014**, *62*, 1221–1234. [CrossRef]
49. Xu, Y.; Lu, C.; Deng, Z.; Liu, Y.F. New Semidefinite Relaxations for a Class of Complex Quadratic Programming Problems. *J. Glob. Optim.* **2023**, *87*, 255–275. [CrossRef]

50. Mitra, S.K.; Kuo, Y. *Digital Signal Processing—A Computer Based Approach*; McGraw-Hill Higher Education: New York, NY, USA, 2006.
51. Cheng, Z.; He, Z.; Liao, B.; Fang, M. MIMO Radar Waveform Design with PAPR and Similarity Constraints. *IEEE Trans. Signal Process.* **2018**, *66*, 968–981. [CrossRef]
52. Varadhan, R.; Roland, C. Simple and globally convergent methods for accelerating the convergence of any em algorithm. *Scand. J. Stat.* **2008**, *35*, 335–353. [CrossRef]
53. Stoica, P.; He, H.; Li, J. New Algorithms for Designing Unimodular Sequences with Good Correlation Properties. *IEEE Trans. Signal Process.* **2009**, *57*, 1415–1425. [CrossRef]
54. Zhang, N.; Golomb, S.W. Polyphase sequence with low autocorrelations. *IEEE Trans. Inf. Theory* **1993**, *39*, 1085–1089. [CrossRef]
55. Martino, A.D. *Introduction to Modern EW Systems*; Artech House: Norwood, MA, USA, 2018.
56. Golay, M. A class of finite binary sequences with alternate auto-correlation values equal to zero. *IEEE Trans. Inf. Theory* **1972**, *18*, 449–450. [CrossRef]